Centrifuge modelling of pipelines shallowly embedded in liquefied submarine slopes

By

Yao Wang

Student number:	4742869	
Project duration:	September 2018 – February 2019	
Thesis supervisor:	Dr. A. (Amin) Askarinejad	TU Delft
	W. (Weiyuan) Zhang	TU Delft

1. Abstract

Marine pipelines are widely used for transporting hydrocarbon material. However, they can be damaged by marine geo-hazards such as seabed liquefaction, as they may sink, float or be dragged by the moving soil. One of the triggering mechanism of seabed liquefaction is the increase of seabed inclination as a result of the souring process or human construction activities. Experiments are carried out to simulate seabed liquefaction and to study the drag forces on a shallowly buried gas pipe at a centrifugal acceleration field of 50g. A tilting mechanism is applied to trigger sample liquefaction. A fluidization system equipped at the bottom of the strongbox is designed to prepare fully saturated, loose and uniform samples. Viscous fluid made of Hydroxypropyl Methylcellulose powder is used as the pore fluid. A hollow model pipe is embedded in the sand layer shallowly with a specific embedment ratio. The pipe fixities are made to be adjustable for adjusting pipe locations horizontally and vertically. Strain gauges attached on fixities are used to monitor the loads exerted on the pipe. The effect of the presence of pipes on the sand layer instability is presented. Furthermore, the drag forces acting on the pipe at a specific embedment ratio is discussed.

2. Introduction

The demand for offshore pipelines increases with expanding offshore oil and gas exploration and extraction activities (Sabbar et al., 2017). Meanwhile, pipeline failures caused by geo-hazards are frequently reported. Seabed liquefaction, as one of the main offshore geo-hazards, can cause significant deformation and failure of pipelines, which may sink, float or be dragged by the moving soil. Getting insight into this natural hazard is essential for developing new design methods of pipelines and minimizing potential catastrophes in the future. In this research, experiments are carried out to simulate the seabed liquefaction and to study the drag forces on a shallowly buried gas pipe at a centrifugal acceleration field of 50g.

In an attempt to achieve good predictions of pipe–soil interaction for shallowly embedded pipelines, a variety of physical model tests under 1g or centrifuge conditions have been performed and the drag forces on the shallowly buried pipelines exerted by surrounding soil have been examined. To simulate the debris flow under prototype scale, Zakeri et al. (2008) built a 0.2m wide and 9.5m long flume suspended inside a tank. The slurry was released from the higher side of the flume and flowed down to the pipe model at the lower side of the flume. The drag forces parallel to the flume bed and perpendicular to the bed were measured. However, the scale of set-up in 1g tests limits the application and reproducibility of the studies. To overcome that, the centrifuge modelling technique has been widely accepted. Zhang et al. (1999) used a cone actuator sitting on the strongbox to generate monotonic vertical and horizontal movements of the pipe model. A moving plate was adopted by Oliveira et al. (2016) to generate soil movements and the amount of induced force on the pipe was measured. Calvetti et al. (2004) adopted another way in which the pipe model was pulled in the direction perpendicular to its axis using a wire and pulley system. In this way, only the horizontal displacement of the tube was controlled. Based on these centrifuge studies, the basic mechanism of interaction between pipe and surrounding soil has been fairly interpreted. However, the relative movement of soil or pipe in these studies were both human-made and the triggering mechanism of liquefaction was not taken into account in their approaches.

This study presents results from physical modelling tests carried out on the geotechnical centrifuge at TUD to investigate the drag forces exerted by induced soil mass movement on the pipeline buried in sand. Fully saturated, loose and uniform samples were prepared and tilted by a linear motor until the liquefaction was triggered. As the innovation in this research, the forces on the pipe model exerted by sand slope flow can be measured directly by strain gauges. Compared with previous methods, the whole process, from liquefaction occurred to sample failure and then forces obtained, was executed by pre-set programs and machines under centrifuge acceleration condition without any artificial intervention so that human-made disturbance can significantly decrease.

Furthermore, inspired by the studies of Cuong et al. (2018), Computed Tomography was introduced to identify the uniformity of the fluidized sample. Moreover, Particle Image Velocimetry (PIV) was conducted to capture the failure mechanism of the samples and at the end, a comparison between experimental and analytical results of drag forces was undertaken.

3. Experimental set-up and sample preparation

3.1. Set-up

The strongbox in Figure 1 is assembled with three aluminum plates (two sides and bottom) and two transparent Plexiglas sheets. The inner dimensions are (length $\times$ width $\times$ height) $380 \times 134 \times 132\ mm^3$ at model scale. A hollow upper-box made of aluminum was fixed on top of the strongbox to ensure sufficient space for the fluid during tilting (Figure 2). Pore pressure transducers (PPTs, MPXH6400A) were fixed in the strongbox for measuring pore pressures at seven positions during testing.

A tilting system has been built for simulating submerged sand slope liquefaction triggered by the increase of slope angle. A linear motor is connected to the frame for tilting the sample inside the strongbox as shown in Figure 2. In the study of Zhang and Askarinejad (2019b) more details of experimental set-up are illustrated.

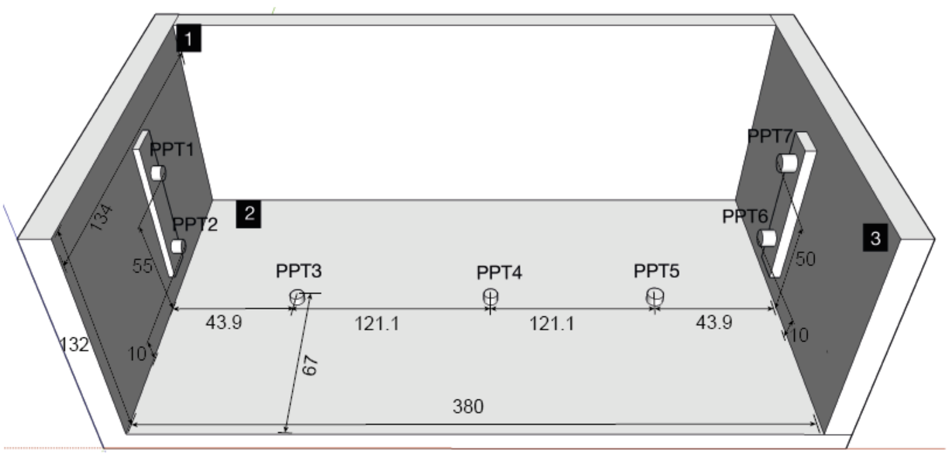

Figure 1. Schematic view of the strongbox and PPTs (model scale: mm): 1) Plexiglas sheet; 2) stainless steel mesh; 3) aluminum plates;

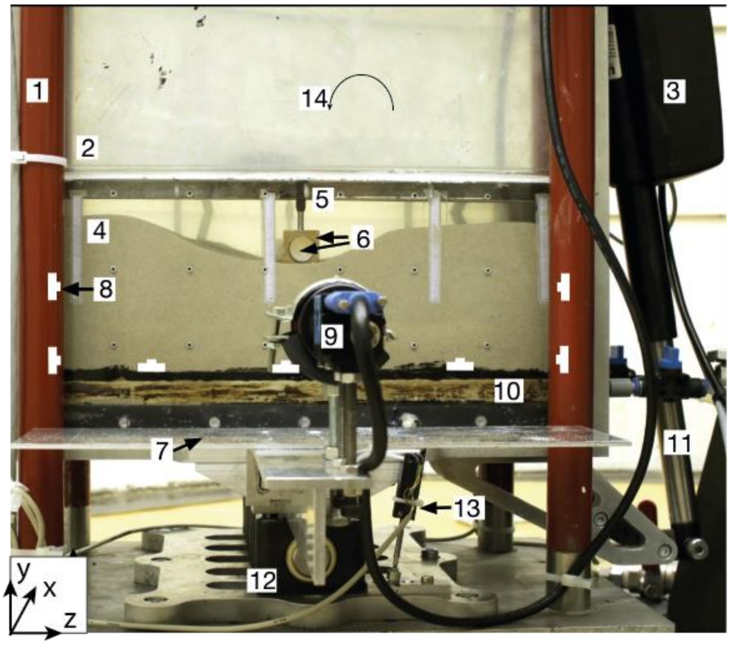

Figure 2. Front view of test set-up before sample preparation: 1) centrifuge basket; 2) upper-box; 3) linear motor; 4) scale; 5) lower rod; 6) pipe model and connecting shafts; 7) lighting board; 8) projections of seven PPTs; 9) high speed camera; 10) frame of fluidization system; 11) valves; 12) rotating axis; 13) linear potentiometer; 14) tilting direction

3.2. Soil material and pore fluid

Geba sand was used in this experiment considering the performance in terms of reproducibility of liquefaction flow slides in the strongbox (de Jager, 2018). Based on the study of Zhang and Askarinejad (2019a), the specific gravity of the sand G_{S} is 2.67; the maximum void ratio $e_{\max}$ and minimum void ratio $e_{\min}$ are 1.07 and 0.64, respectively, and the effective residual friction angle of the sand $\varphi'_{\mathrm{residual}}$ is $36°$. The uniformity coefficient C_{u} is 1.55 and the coefficient of curvature C_{c} is 1.24.

Under Ng condition, viscous fluid, which is used as submerging fluid, is necessary for simulating static liquefaction. Take et al. (2004) believed that the internal mechanism leading to static liquefaction can be explained by the collapse of saturated void, which results in local and abrupt increase of the pore pressure. Therefore, Askarinejad et al. (2014) propose that the scaling factor for pore fluid should be derived based on grain scale. Following the time scaling factors for generation (Equation 1) and dissipation (Equation 2) of excess pore pressure at grain scale, the viscosity of the fluid should be $\sqrt{N}$times that of water.

$$T_{\mathrm{r}}^{\mathrm{generation}} = \frac{T_{\mathrm{p}}^{\mathrm{generation}}}{T_{\mathrm{m}}^{\mathrm{generation}}} = \sqrt{N} \quad 1$$

$$T_{\mathrm{r}}^{\mathrm{dissipation}} = \frac{T_{\mathrm{p}}^{\mathrm{dissipation}}}{T_{\mathrm{m}}^{\mathrm{dissipation}}} = N \quad 2$$

where $T^{\mathrm{generation}}$ is the time of the generation of excess pore pressure caused by the gravitational falling at a particle grain scale; $T^{\mathrm{dissipation}}$ is the time of the dissipation of excess pore pressure based on Darcy' s law at grain scale; the subscripts *p* and *m* stand for prototype and model, respectively, and the subscript *r* represents the scaling ratio (prototype/model). Hence, viscous fluid with kinematic viscosity of $\sqrt{N}$ (7.07) cSt was applied, where *N* is 50 in this study. The fluid was made of E10M Hydroxypropyl Methylcellulose (HPMC) powder. The density of the viscous fluid is assumed to be the same as that of water, since the HPMC concentration is less than 1%.

3.3. Pipe model

Based on the design of typical gas pipes in practice (Folga, 2007), a pipe with a diameter (*D*) of 0.9 m at prototype scale was selected. A special load measuring system was designed, including a top beam, two adjustable rods, strain gauges and a pipe model (Figure 3). The top beam was fastened to the top of the strongbox to keep the system still during the tilting. The different pipe embedded ratios are fulfilled by changing the length of threaded rods as shown in Figure 4, where *H* is the embedded depth (to axis) of the pipe and *D* is the diameter of the pipe.

Horizontal drag force on the pipe exerted in z direction (Figure 4) was measured by a set of strain gauges fixed on the upper part. Strain gauges attached just above the pipe can measure the forces in y direction (Figure 3).

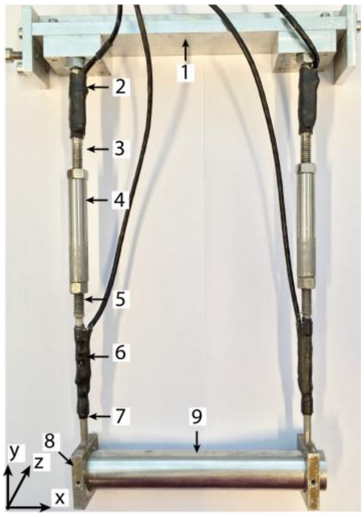

Figure 3. Load measuring system 1) top beam; 2) upper strain gauges for measuring load in z-direction; 3) upper threaded rod; 4) internally threaded rod; 5) lower threaded (left direction) rod; 6) lower strain gauges for measuring load in y-direction; 7) lower rod; 8) pipe connection 9) pipe model

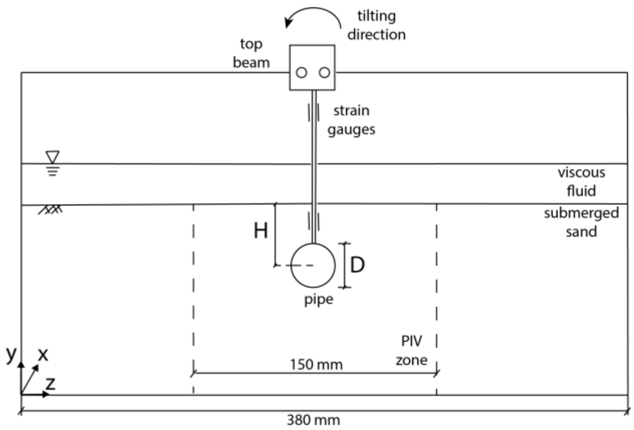

Figure 4. Schematic view of the load measuring system

4. Results & Discussion

In this study, one centrifuge test was conducted twice to validate the reproducibility of the experiment as illustrated in Table 1. $Dr_{1\mathrm{g}}$ and $Dr_{50\mathrm{g}}$ in Table 1 are the relative densities of the samples measured at 1g and 50g conditions, respectively; γ' is the buoyancy unit weight of saturated sand sample; θ_{f} is the failure angle of the sample.

The tests started with a fully submerged sand sample that was fluidized during the first stage. After re-sedimentation of the loose sand started, the pore pressure dissipated within a few minutes. Next, the centrifuge was gradually accelerated to 50g and the tank was tilted to the final failure angle.

Table 1. Details of the three centrifuge tests

Test name	Tilting rate (°/s)	g-level (g)	Dr_{1g} (%)	Dr_{50g} (%)	Embedment ratio (*H*/*D*)	γ' (kN/m^3)	θ_f (°)
Cen1	0.1* (0.002**)	50	31	61	0.8	9.1	11.97
Cen2	0.1* (0.002**)	50	30	64	0.8	9.1	12.59

*: model scale; **: prototype scale

4.1. Uniformity of the sample

Knowing the sample uniformity is essential for evaluating sample properties. The uniformity of the sample made by the fluidization method was examined by the Siemens SOMATOM Volume zoom CT scanner at Delft University of Technology. There is a linear relationship between the CT_{number}, which is transformed from Hounsfield Units, and the bulk density of the scanned material. Based on that, Zhang and Askarinejad (2019b) proposed a function in which the void ratio of the scanned material can be obtained from the CT_{number} as shown in Equation 3, where 0.001 and 0.0146 are calibration coefficients in this study.

$$\mathrm{e} = \frac{G_s - 1}{0.001 \cdot CT_{\mathrm{number}} + 0.0146} - 1 \qquad 3$$

To minimize disturbance exerted by the movement of the strongbox during the scan, a section of the sample measured 14.4 mm at model scale between PPT 4 and PPT 5 was scanned to measure the variation of relative density with depth and width after fluidization without moving the strongbox (Figure 5).

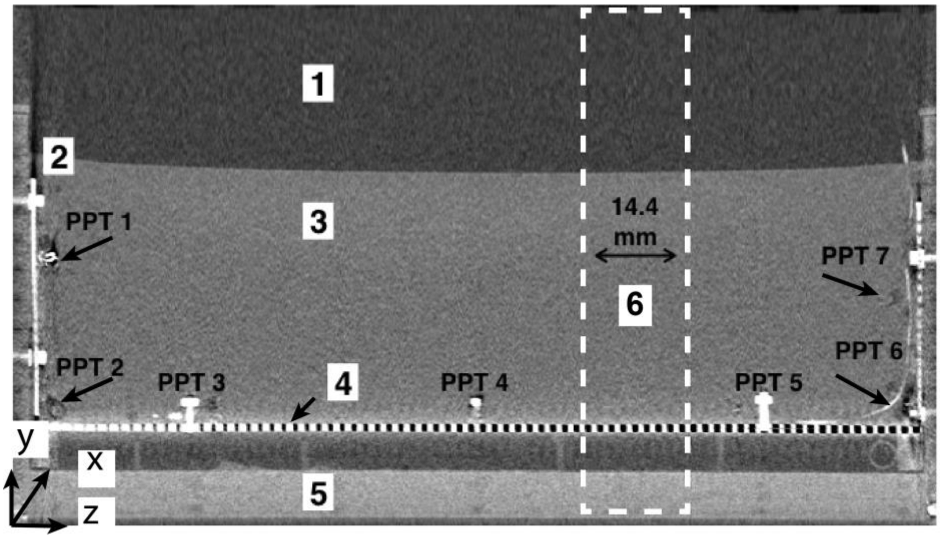

Figure 5. Longitudinal cross section view of strongbox (32-bit) (model scale): 1) viscous fluid; 2) stainless steel frame to fasten PPTs; 3) submerged sand; 4) stainless steel meshes and filter; 5) bottom of the strongbox made of aluminum; 6) scanned zone

Figure 6 illustrates the distribution of relative density of the sample in Cen1 over the width after fluidization. It is shown that the average relative density decreases to roughly 30% via fluidization. It is noted that a higher relative density along boundaries is caused by the friction of walls and relative low discharge of fluidization around boundaries.

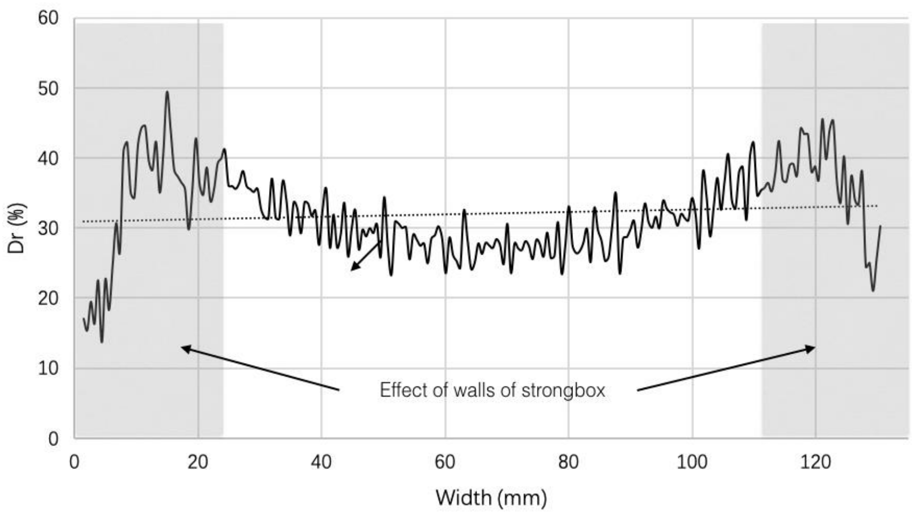

Figure 6. Variation of relative density of sample over width

The variation of relative density over depth is represented in Figure 7. Considering the beam hardening effect (light streaks near the metallic frame at the bottom in Figure 8), only the top 77 mm of sample is interpreted here. An extreme loose layer of 10 mm is believed that the smaller particles in the sample tend to be pushed further up during fluidization than the larger ones, while the setting velocity is smaller. The average relative density of the underlying uniform layer of roughly 50 mm is 33%, which agrees with the results over width. The increase of relative density from 60 mm depth is mainly caused by the beam hardening effect, which makes the value of the bottom part unreliable.

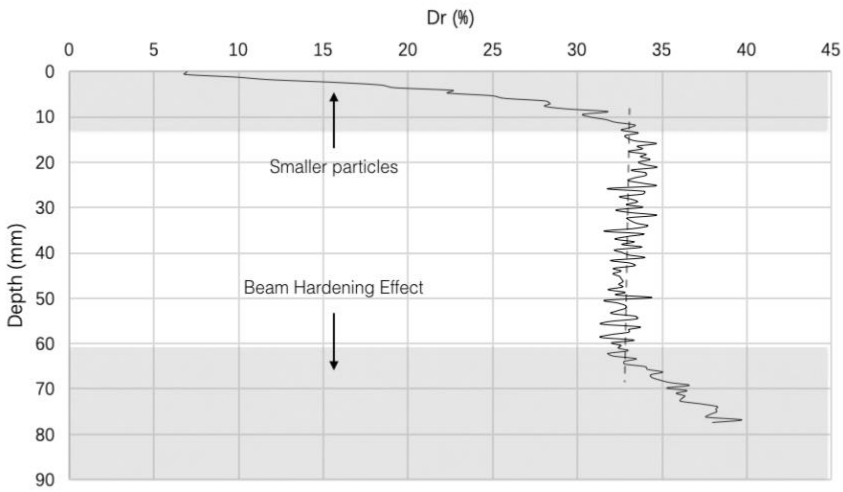

Figure 7. Variation of relative density over depth (model scale)

Figure 8 shows the transition of sample before and after the disturbance exerted by moving the strongbox, in which light parts represent material with higher density. It demonstrates that the central part of the sample was rarely influenced by the disturbance. It is worth noting that the different display modes in Figure 5 and 8 are simply for the convenience of interpretation and they were derived from the same CT scan result. Figure 5 is displayed in 32-bit mode to gain a better illustration of the inner view of the strongbox. Figure 8 is set to 16-bit and the contrast is enhanced to make beam hardening effect and densification easier to be observed.

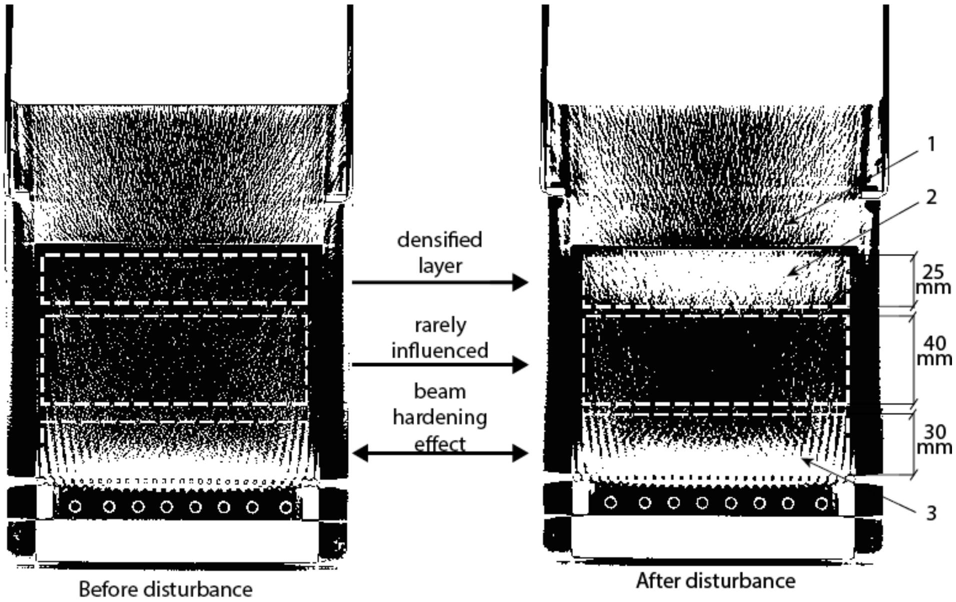

Figure 8. The transition of the sample because of disturbance (16-bit): 1) viscous fluid; 2) denser sand layer; 3) beam hardening effect

Based on analysis of relative density in two main directions of sample, which show good agreement with each other. it is proved that the fluidization system is capable of producing uniform loose sand sample.

4.2. PIV interpretation

Particle Image Velocimetry (PIV) technique was adopted to illustrate the process of liquefaction in Cen1 as shown in Figure 9. The frequency of the high-speed camera was set to 30 frames per second. Figure 9a records the initial stage of liquefaction and Figure 9b and 9c are the soil movement 0.067 s and 0.13 s later respectively, at prototype scale, which were the second and the third frame followed Figure 9a. Shown in Figure 9a, the particles around the pipe moved 12.5mm at prototype scale in the first 1/30s, which means that, the velocity of the adjacent particles around the pipe was around 0.375 m/s at prototype scale. It is demonstrated that the obvious soil movement occurred firstly in the vicinity (downstream direction) of the pipe, then the movement spread to the downstream of the pipe and near the slope toe. After that, the trend spread to the whole sample and large movement occurred.

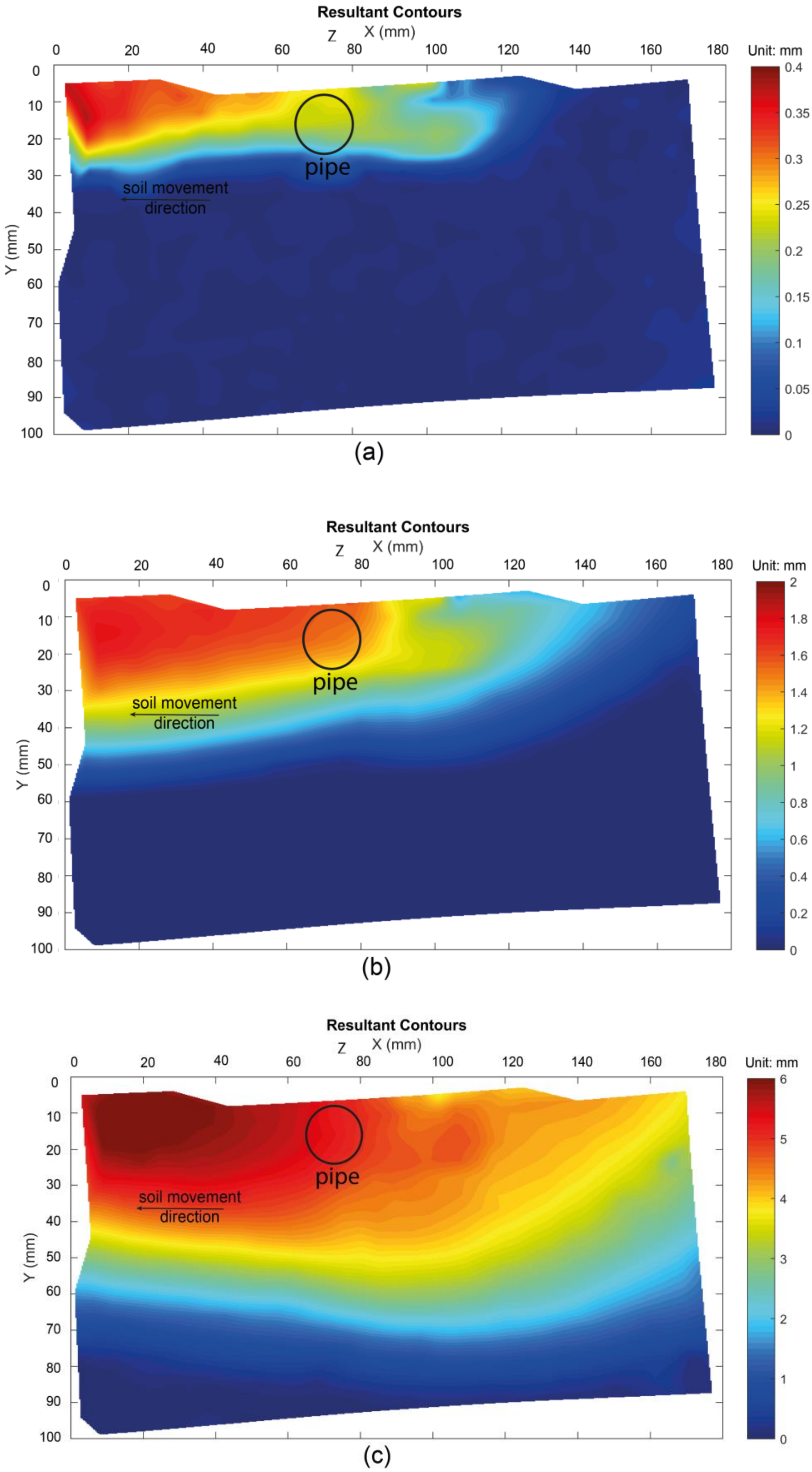

Figure 9. Sand element displacement contours during liquefaction by PIV

4.3. Excess pore pressure

The relative densities of samples of Cen1 and Cen2 are 61% and 64%, respectively, measured before tilting (Table 1), which are far larger than the result of CT scan. It is believed that the process of enhancing centrifuge acceleration increased the effective stress of the sample, which made the sample compressed.

The change of values of excess pore pressure at seven measure points during tilting in Cen1 is illustrated in and exact values of excess pore pressure ratios at seven measure points when the liquefaction was triggered are listed in Table 2. The pore pressure ratio r_{u} is defined as the excess pore fluid pressure p_{exc} divided by effective stress of the element σ_0' as shown in Equation 4 (Jiaer et al., 2004). The excess pore fluid pressures p_{exc} for each of seven measure points are calculated by Equation 5, where p_{k} is the measured pore fluid pressure for Cen1 ($k = 1,2,3, \ldots ,7$); $p_{\mathrm{h\_k}}$ is the hydrostatic fluid pressure at the position of measurement.

$$r_{\mathrm{u}} = \frac{p_{\mathrm{exc}}}{\sigma_0'} \qquad 4$$

$$p_{\mathrm{exc}} = p_{\mathrm{k}} - p_{\mathrm{h\_k}} \qquad 5$$

In Figure 10, it is illustrated that PPT1 and PPT2 instantly and simultaneously rise at a tilting angle of approximately 11.97°, marking the start of instability. The excess pore pressures at the middle of the slope, measured by PPT4 and PPT5, increased 0.01s later and the reading of PPT6 and PPT7, which located at the crest of the slope, rose eventually but values were smaller than others. It is clear that, in Cen1, the failure occurred at the tilting angle of 11.97° for almost the whole sample and the toe of the slope first reached liquefaction state. The results of PPTs show the same trend of failure procedure with the analysis from PIV.

The values of pore pressure ratios at seven measure points in two experiments are illustrated in Table 2. Although values of Cen2 are smaller than those of Cen1, two tests show the same trend of pore pressure ratios with respect to configurations of PPTs when liquefaction was triggered, which proves the reproducibility of the experiment. The excess pore pressure ratio at PPT1 in both two tests exceed 1. It is believed that the dynamic effect of slope movement made the excess pore pressure at PPT1 exceed the effective stress at the point.

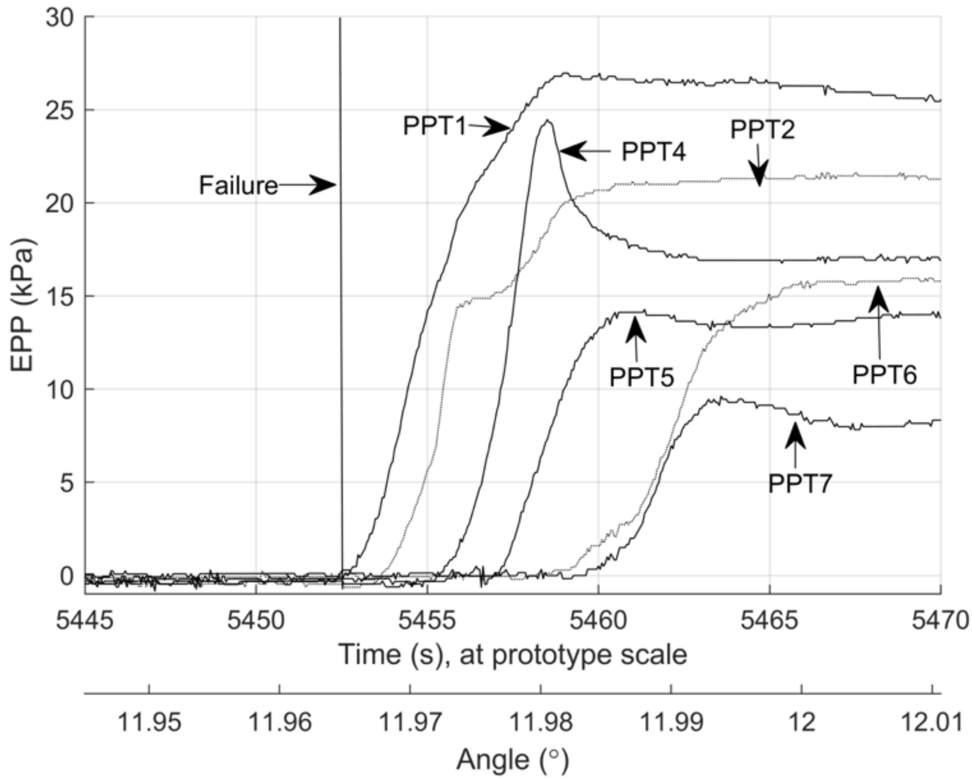

Figure 10. Excess pore pressure (EPP) of Cen1 when the liquefaction initiated

Table 2. Excess pressure ratios at the area of PPTs

	PPT1	PPT2	PPT3*	PPT4	PPT5	PPT6	PPT7
Cen1	1.26	0.73	0.64	0.64	0.59	0.52	0.42
Cen2	1.10	0.54	0.46	0.58	0.34	0.40	0.37

*: based on slow channel which has a data logging rate of 3 HZ

4.4. Drag pressure

Current methods to quantify the impact forces caused by a slide on a pipeline can be divided into the geotechnical and fluid dynamic approaches. At the onset of a submarine slope failure, the failed mass shifts initially at low velocity, and possesses geotechnical properties close to those of the pre-failure soil mass. The slide drag pressure q_{ult} exerted on the pipe can be estimated from the Equation 6 (Trautmann and O'Rourke, 1985),

$$q_{ult} = \gamma' \cdot N_{\mathrm{q}} \cdot H \qquad 6$$

where γ' is the buoyancy unit weight of saturated sand sample; H is the embedded depth, which is 0.72m at prototype scale; the ultimate bearing capacity factor N_{q} are both 3.5 for Cen1 and Cen2, estimated by the curve proposed by Brinch-Hansen (1961).

In this experiment, the surface of the sand bed changed from the flat ground surface condition to a slope with respect to the position of the pipe because of tilting. Therefore, Equation 6 cannot be applied directly due to this geometric difference. Based on the theory of Audibert and Nyman (1977), Zhang and Askarinejad (2019a) suggested Equation 7 to consider the effect of slope angle, where the pipe centre to slope crest distance (L_c) is 9.5 m at prototype scale; when $\theta_{\mathrm{f}} = 12.59°$, the weight factor, ω, is 0.83 and N_q is 3.1; when $\theta_{\mathrm{f}} = 11.97°$, ω is 0.84 and N_q is 3.1.

$$q_{\mathrm{us}} = \gamma' \cdot D \cdot \left(\frac{H}{D}\right)^{\omega} \cdot \left(\frac{D}{L_{\mathrm{C}}}\right)^{1-\omega} \cdot N_{\mathrm{q}} \qquad 7$$

As the failed soil mass travels further downslope, remolding of the soil and interaction with the surrounding water takes place (Zakeri, 2009). Although a debris flow has low shear strength, the inertial drag force exerted by the slide materials is sufficiently large to cause damage to a pipeline (Sahdi et al., 2014). For this situation, the geotechnical approach based on the soil strength (Equation 6) is inadequate.

A common approach to assess the impact load from a debris flow is to characterize the flow as a non-Newtonian fluid (Zakeri et al., 2008). The slide impact force F_{D} can be estimated by Equation 9. The density of the debris ρ is 1917 $\mathrm{kg/m^3}$; the free upstream velocity U_∞ is 60mm/s; the drag coefficient C_D for laid-on-seafloor pipe is adopted as shown in Equation 10, considering the shallowly embedded condition and the value is 1.8; the Reynolds number is 13.38.

$$q_\mathrm{ult} = \frac{1}{2}\rho \cdot C_\mathrm{D} \cdot U_\infty^2 \tag{8}$$

$$C_\mathrm{D} = 1.25 + \frac{11.0}{Re_{\mathrm{non-Newtonian}}^{1.15}} \tag{9}$$

The changes of the horizontal stress on the pipe model exerted by the surrounding soil in Cen1 and Cen2 were illustrated in Figure 11. For Cen1, at a tilting angle of approximately 11.9°, the horizontal stress on the pipe promptly jumps to 9.8 kPa. For Cen2, the angle and horizontal stress are 12.1° and 10.1 kPa, respectively.

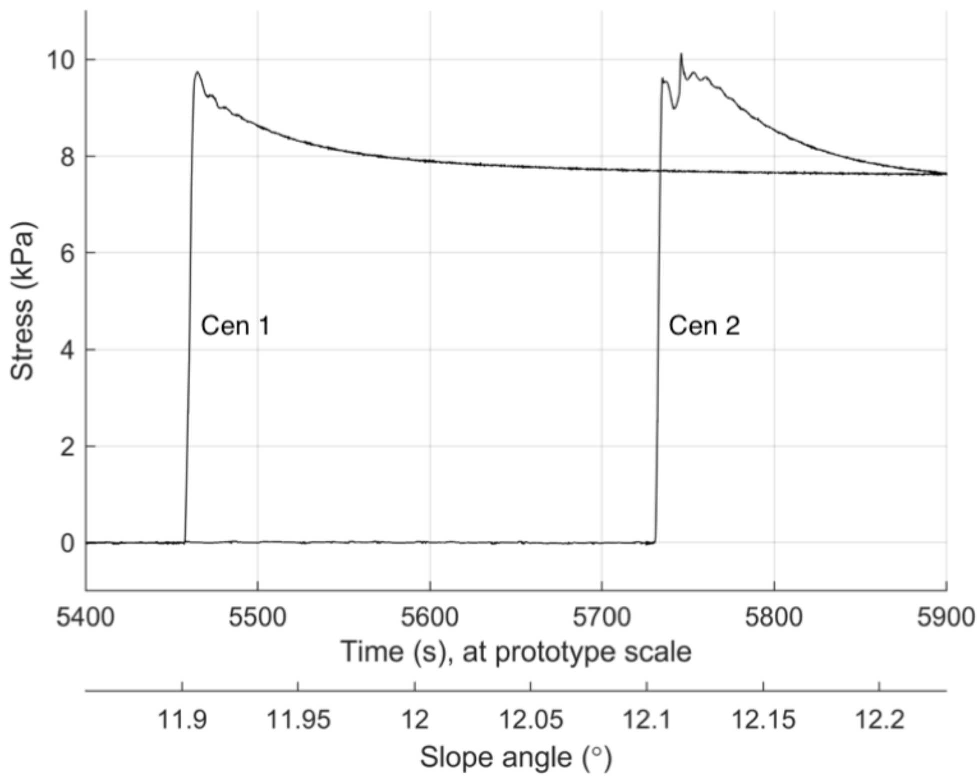

Figure 11. Horizontal stress on the pipe in Cen1 and Cen2 at prototype scale with increasing slope angle

A comparison between analytical results and experimental results have been illustrated in Table 3. Both geotechnical methods overestimate the ultimate external pressure. The consideration of geometric influence in the method proposed by Zhang and Askarinejad (2019a) improves the estimation but theories simply based on empirical coefficient N_q are still not adequate for complex failure situations. More factors like strain-rate effects on the undrained shear strength of the moving soil shall be included. Besides, the fluid dynamic method underestimates the result. It indicates that the sample is not fully fluidized at the beginning of liquefaction and the real situation shall be between these two scenarios where the sample lose part of its shear strength.

Since the vertical component of drag was too small to be measured, only the horizontal component of drag force was interpreted.

Table 3. Comparison between analytical and experimental results

Author(s) – Year	Method	Formulas	External pressure (kPa)
Trautmann and O'Rourke (1985)	Conventional Geotechnical Method	$q_{ult} = \gamma' \cdot \mathrm{H} \cdot N_q$	39.74
Zhang and Askarinejad (2019a)	Geotechnical Method*	$q_{ult} = \gamma' \cdot D \cdot \left(\frac{H_C}{D}\right)^{\omega} \cdot (\frac{D}{L_C})^{1-\omega} \cdot N_q$	27.73($\theta_f = 12.44°$) 26.86 ($\theta_f = 12.44°$)
Zakeri et al. (2008)	Fluid Dynamic Method	$q_{ult} = \frac{1}{2}\rho \cdot C_D \cdot U_\infty^2$	9.43
Experimental test	Centrifuge modelling	–	9.8 (Cen1) 10.1 (Cen2)

* Considering the effect of slope ground condition based on Geotechnical Method

5. Conclusion

In this study, the strongbox with fluidization system used to prepare loose, fully saturated and uniform sand samples was demonstrated and a novel force measurement system developed for this study was tested. The results of physical tests and analytical computations of the drag force on a shallowly embedded pipeline induced by sand liquefaction have been illustrated and compared. The uniformity of the fluidized sample was tested by tomography technique. Besides, PIV approach was adopted for interpretation of failure mechanism of the sample. The main conclusions are presented below:

1) The agreement between analytical results and experimental results proves that the new apparatus is capable of reproducing liquefaction flow slides and measuring the drag forces successfully.
2) The movement of the sample follows the fluid dynamic theory, which means that the sand sample lost its strength immediately when the failure occurred.
3) The liquefaction was triggered by the local failure occurred in vicinity of the pipe and then the tendency of movement spread to the downstream of the pipe. The slope toe failure was firstly measured by the PPT.

6. Reference

ASKARINEJAD, A., BECK, A. & SPRINGMAN, S. M. 2014. Scaling law of static liquefaction mechanism in geocentrifuge and corresponding hydromechanical characterization of an unsaturated silty sand having a viscous pore fluid. *Canadian Geotechnical Journal,* 52**,** 708-720.

AUDIBERT, J. M. & NYMAN, K. J. 1977. Soil restraint against horizontal motion of pipes. *Journal of the Geotechnical Engineering Division,* 103**,** 1119-1142.

BRINCH-HANSEN, J. 1961. The ultimate resistance of rigid piles against transversal forces. *Geoteknisk Instit., Bull.*

CALVETTI, F., DI PRISCO, C. & NOVA, R. 2004. Experimental and numerical analysis of soil–pipe interaction. *Journal of geotechnical and geoenvironmental engineering,* 130**,** 1292-1299.

CUONG, N. L. Q., MINH, N. H., CUONG, H. M., QUOC, P. N., VAN ANH, N. H. & VAN HIEU, N. 2018. Porosity Estimation from High Resolution CT SAN Images of Rock Samples by Using Housfield Unit. *Open Journal of Geology,* 8**,** 1019.

DE JAGER, R. 2018. Assessing Liquefaction Flow Slides: Beyond Empiricism.

FOLGA, S. 2007. Natural gas pipeline technology overview. Argonne National Lab.(ANL), Argonne, IL (United States).

JIAER, W., KAMMERER, A., RIEMER, M., SEED, R. & PESTANA, J. Laboratory study of liquefaction triggering criteria. 13th world conference on earthquake engineering, Vancouver, BC, Canada, Paper, 2004.

OLIVEIRA, J. R. M., RAMMAH, K. I., TREJO, P. C., ALMEIDA, M. S. & ALMEIDA, M. C. 2016. Modelling of a pipeline subjected to soil mass movements. *International Journal of Physical Modelling in Geotechnics,* 17**,** 246-256.

SABBAR, A. S., CHEGENIZADEH, A. & NIKRAZ, H. 2017. Static liquefaction of very loose sand–slag–bentonite mixtures. *Soils and Foundations,* 57**,** 341-356.

SAHDI, F., GAUDIN, C., WHITE, D., BOYLAN, N. & RANDOLPH, M. 2014. Centrifuge modelling of active slide-pipeline loading in soft clay. *Géotechnique,* 64**,** 16.

TAKE, W., BOLTON, M., WONG, P. & YEUNG, F. 2004. Evaluation of landslide triggering mechanisms in model fill slopes. *Landslides,* 1**,** 173-184.

TRAUTMANN, C. H. & O'ROURKE, T. D. 1985. Lateral force-displacement response of buried pipe. *Journal of Geotechnical Engineering,* 111**,** 1077-1092.

ZAKERI, A. 2009. Submarine debris flow impact on suspended (free-span) pipelines: Normal and longitudinal drag forces. *Ocean Engineering,* 36**,** 489-499.

ZAKERI, A., HØEG, K. & NADIM, F. 2008. Submarine debris flow impact on pipelines—Part I: Experimental investigation. *Coastal engineering,* 55**,** 1209-1218.

ZHANG, J., RANDOLPH, M. & STEWART, D. An elasto-plastic model for pipe-soil interaction of unburied pipelines. The Ninth International Offshore and Polar Engineering Conference, 1999. International Society of Offshore and Polar Engineers.

ZHANG, W. & ASKARINEJAD, A. 2019a. Behaviour of buried pipes in unstable sandy slopes. *Landslides,* 16**,** 283-293.

ZHANG, W. & ASKARINEJAD, A. 2019b. Centrifuge modelling of submarine landslides due to static liquefaction. *Landslides (Under Review)*.